ROYAL SOCIETY
OF CHEMISTRY

PAPER

Check for updates

Innovating carbon-based perovskite solar cells: the role of a CN-anchoring self-assembled molecular layer in efficiency and stability†

Sheida Rezakhani,[a] Hashem Shahroosvand, [ID] *[a] Peng Gao[b] and Mohammad Khaja Nazeeruddin [ID] *[cd]

The discovery of self-assembled molecular layers (SAMLs) containing anchoring groups such as COOH and PO_3H as efficient hole-selective materials (HSMs) in p–i–n perovskite solar cells (PSCs) is pivotal to enhancing the interaction between HSMs and perovskite layers. In this work, we propose, for the first time, an HSM featuring CN groups as anchoring groups in n–i–p devices, achieving a maxmium power conversion efficiency (PCE) of 20.37% (mean value = 19.83%) using a carbon electrode. The HSM is based on a phenanthroimidazole backbone linked to aza and cyanide groups. VASP computational studies reveal that the new HSM can coordinate to Pb atoms in the perovskite layer through CN groups in a bridging mode (where two CN groups bond to two Pb atoms), with an adsorption energy (E_{ads}) of −1.04 eV. These SAMLs demonstrate greater stability compared to the classic spiro-OMeTAD, with a remarkable one-year operational stability. The photostability and thermal stability of PSCs incorporating the new SAMLs are notable, retaining approximately 97.5% of their initial PCE after 600 hours at 80 °C under ambient conditions. Additionally, the devices have exhibited impressive visual stability for over one year. The operational stability of PSCs based on carbon electrodes, combined with the versatility of CN-functionalized organic molecules, positions these materials as promising candidates for the large-scale production of PSCs with metal-free electrodes, eliminating the need for thermal evaporation techniques. Our findings represent a paradigm shift from conventional spiro-OMeTAD-based hole transporting materials to novel SAML-based HSMs, paving the way for advancements in PSC technology.

1. Introduction

Hole transport materials (HTMs) in perovskite solar cells (PSCs) play a key role in achieving high power conversion efficiencies (PCEs) by reducing recombination at the interface between the perovskite and the contact layer. A variety of HTMs – ranging from small molecules to polymers and p-type inorganic semi-conductors – have been extensively investigated in PSCs.[1–3] Recent advancements in the field have highlighted the potential of anchoring groups containing self-assembled molecular layer (SAML) materials as efficient hole-selective materials (HSMs). As an interface engineering strategy, SAMLs can effectively serve as HSMs to replace the conventional HTMs in PSCs, leveraging their structural advantages to optimize the device efficiency.[4–7] We abandoned the term 'self-assembled monolayers' because they are proven to be not a monolayer. SAML HSMs promote smooth morphology and improved crystallinity of the perovskite film by adsorbing spontaneously onto the substrate surface, thereby enhancing the device performance.[8] Moreover, SAMLs modulate the surface dipole moment, impacting charge transfer and recombination dynamics. They facilitate homogeneous perovskite layer formation, resulting in improved fill factor (FF) and open-circuit voltage (V_{OC}).[9,10] SAMLs also boast advantages such as solubility in environmentally friendly solvents, reduced biotoxicity, minimal material consumption, straightforward fabrication processes, and excellent reproducibility.[11]

Typically, SAMLs comprise three components: (i) an anchoring group with a strong affinity for the substrate; (ii) a linker group that facilitates molecular ordering through noncovalent interactions; and (iii) a terminal group responsible for charge transport.[12,13] The selection of the anchoring group is critical, as it influences the binding energy, surface dipole moment, charge transfer, and recombination in the device.

[a]Group for Molecular Engineering of Advanced Functional Materials (GMA), Chemistry Department, University of Zanjan, Zanjan, Iran. E-mail: shahroos@znu.ac.ir

[b]Laboratory for Advanced Functional Materials, Xiamen Institute of Rare Earth Materials, Haixi Institute, Chinese Academy of Sciences, Xiamen 361021, China. E-mail: p_gao@foxmail.com

[c]Group for Molecular Engineering of Functional Materials, Institute of Chemical Sciences and Engineering, École Polytechnique Fédérale de Lausanne, CH-1951 Sion, Switzerland. E-mail: mdkhaja.nazeeruddin@epfl.ch

[d]School of Integrated Circuits, Southeast University, Wuxi, Jiangsu, 214026, P. R. China

† Electronic supplementary information (ESI) available. See DOI: https://doi.org/10.1039/d5ta02440d

Common anchoring groups include phosphonic acid (PA), carboxylic acid (CA), cyanoacetic acid (CAA), and cyanoacrylic acid.[14,15]

Pb^{2+} cation related deep-level defects in the perovskite layer significantly contribute to non-radiative recombination, hampering charge transfer and promoting photochemical degradation at the interface.[16] To mitigate these issues, it is essential to employ compounds that reduce such defect densities. Cyano groups are known to act as a Lewis base, forming coordination bonds with Pb^{2+} ions on the perovskite surface, enhancing the performance.[17,18] Several cyano-containing HTMs with commendable efficiencies have been reported, as summarized in the ESI.†

Among organic photovoltaic materials, azo dyes are particularly notable and have been utilized in dye-sensitized, organic, and perovskite solar cells.[19] Derivatives of azo compounds that exhibit donor–π–acceptor (D–π–A) structures display excellent photovoltaic properties due to their extensive π-delocalized systems, where minor modifications in donor or acceptor groups can significantly impact photo-physical and photo-chemical characteristics.[20,21]

In this study, we synthesized a new diazo compound, diCNq-Aza, with a D–π–A structure as an SAML-type HSM (SAML-HSM) and investigated its application in PSCs. The synthetic pathway for producing this compound is straightforward, requiring no expensive purification techniques or costly organometallic catalysts, leading to significant cost reductions. Notably, this HSM does not necessitate chemical oxidation or the incorporation of doping agents such as LITFSI and *t*-butyl pyridine to achieve high PCEs, making it a promising alternative for use in n–i–p type PSCs. We employed a combination of theoretical and experimental approaches to investigate the electronic properties of the new HSM and to understand the electron distribution within the designed structure. The CN group as the anchoring moiety bond to two Pb atoms in a bridging mode, which enhances charge transfer and effectively passivates the perovskite. The PCE of the PSC using the carbon electrode surpassed that of spiro-OMeTAD based devices, achieving approximately 21% PCE, one of the highest reported for carbon-based PSCs. Additionally, the PSC with the new SAML retained over 95% of its initial performance over time – especially at 80 °C – demonstrating exceptional thermal stability. Notably, the PSC showed no signs of decomposition after one year, whereas the fresh perovskite deteriorated within one month. This work paves the way for competitive carbon-based PSCs through integration of the new CN-functionalized SAML-HSM with carbon electrodes.

2. Results and discussion

2.1 Optical, electrochemical and thermoanalytical properties

A new SAML-HSM was synthesized by using two sequential pathways to obtain primary compounds **3** and **4**, resulting in
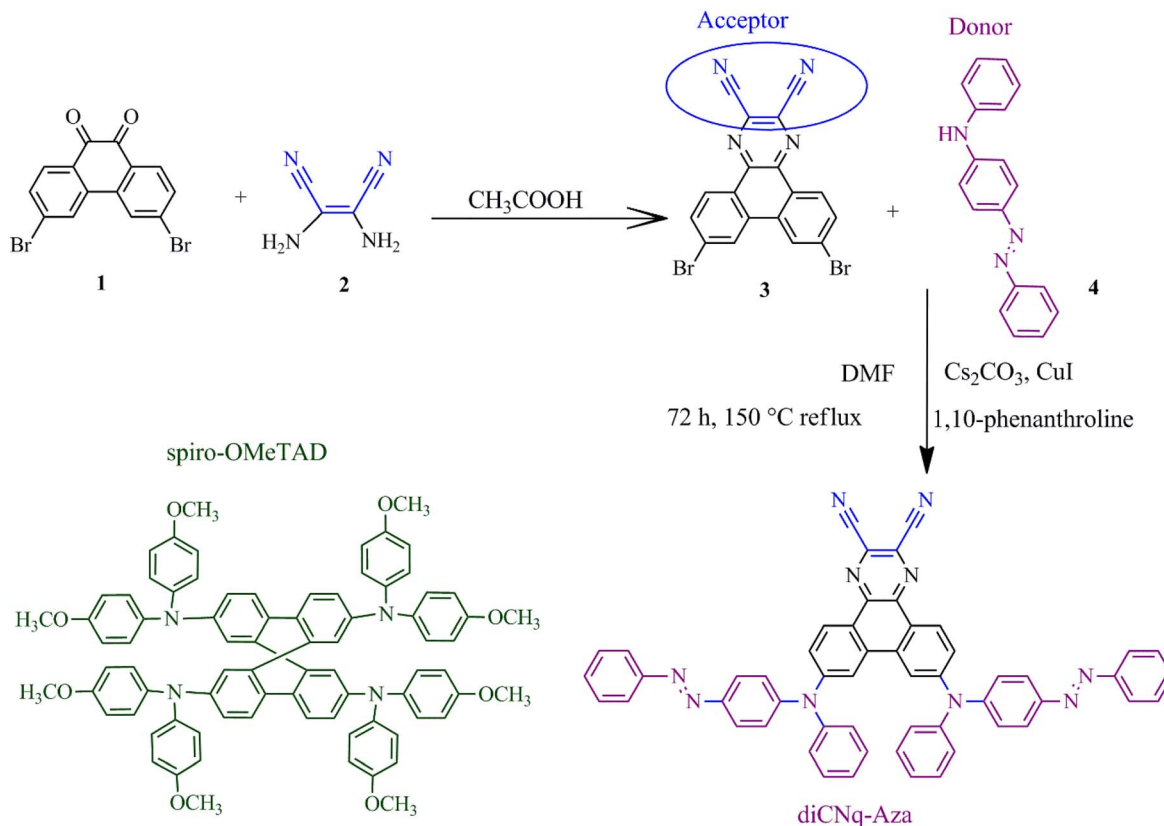

Fig. 1 Synthesis reactions and molecular structures. Schematic illustration of the overall reaction mechanism for the formation of diCNq-Aza and spiro-OMeTAD.

a C–N coupling to produce diCNq-Aza. In contrast to the routine strategy for preparing C–N coupling by using the Suzuki method based on a Pd catalyst, the use of Cs_2CO_3/CuI/1,10-phenanthroline dramatically reduced the total cost of the product. In fact, the cost of 1 g of catalyst for the synthesis of spiro-OMeTAD was estimated to be about 68.5 \$, while for the new SAML-HSM diCNq-Aza it reduced to 2.53 \$.

The molecular structures and the synthesis steps of the new SAML diCNq-Aza are illustrated in Fig. 1 and explained in more detail in the Experimental part and ESI.† The new SAML-HSM was fully characterized by spectroscopic methods. ^{1}H-NMR and FTIR spectra of the precursors and the final compound are given in the ESI (Fig. S1 and S2†).

The interesting molecular structure aspect of the new SAML is the presence of Aza groups, which are linked to diphenyl electron donor moieties, as well as CN acceptor groups, which act as anchoring groups, confirming the D–A structure, which acts as an SAML-HSM. In the following sections, we will first prove the D–A properties of the HSM and prove the interaction between CN groups of the SAML and Pb atoms on the surface of perovskite, then will show which coordination mode of the CN group of the new SAML is favored to bind to the perovskite layer using VASP computational studies and finally the calculation of photovoltaic and stability behavior compared to classic spiro-OMeTAD.

To evaluate the band gaps and energy levels of the new SAML-HSM and spiro-OMeTAD molecules, further studies, including optical absorption, light emission, and cyclic voltammetry analysis, were performed. The ultraviolet-visible (UV-vis) absorption and photoluminescence (PL) emission spectra of diCNq-Aza in acetonitrile are shown in Fig. 2a, and the corresponding parameters are listed in Table 1. Two absorption bands are observed at $\lambda_{max} = 296$ and 436 nm; the first one could be attributed to the n–π* transition of aromatic cycles, and the second could be assigned to the π–π* transitions of the π–electron system.[22] Because the new SAML-HSM showed weak light harvesting in the visible region, it could not interfere with the light absorption by the perovskite layer.[23] Surprisingly, the wavelength maximum of the new SAML-HSM red-shifted to about 48 nm compared to spiro-OMeTAD ones, and the optical band gap (E_g) was 0.57 eV less than that of spiro-OMeTAD, which means that the intersection wavelength point consequently shifted to a higher wavelength.

Furthermore, the PL spectrum of diCNq-Aza displays the maximum emission at $\lambda_{max.\ em} = 583$ nm, which moved to a higher wavelength of about 160 nm compared to spiro-OMeTAD ($\lambda_{max.\ em} = 423$ nm), which can be attributed to the presence of strong CN π-acceptor properties as well as the extension of the π conjugated system. Finally, the intersection wavelength of the UV-vis and PL spectra of HSM was used to obtain band gap energy values, which are required to calculate the energies of the lowest unoccupied molecular orbital (E_{LUMO}) for the HSM. The obtained E_g for diCNq-Aza was 2.44 eV and had a smaller band gap than spiro-OMeTAD with $E_g = 3.01$ eV, favoring the thermal population of the conduction band and thus increasing the number of intrinsic charge carriers.[24]

Cyclic voltammetry (CV) analysis was carried out to investigate the electrochemical properties of diCNq-Aza and the estimation of energy levels based on the standard equations.[25] As shown in Fig. 2b, the diCNq-Aza HSM exhibited quasi-reversible oxidation/reduction waves in the positive potential range like spiro-OMeTAD, which indicates its good electrochemical stability in solution. Comparing the electrochemical data for diCNq-Aza and spiro-OMeTAD, it is apparent that the first oxidation half-wave of diCNq-Aza shifted to a lower potential compared to spiro-OMeTAD. Hence, diCNq-Aza was more easily oxidized to diCNq-Aza$^+$ than spiro-OMeTAD oxidation to spiro-OMeTAD$^+$. The estimated values for the highest occupied molecular orbital energies (E_{HOMO}) of diCNq-Aza and spiro-OMeTAD were −5.17 eV and −5.18 eV, respectively, from the equation $E_{HOMO} = -(E_{1/2}$ (vs. Fc/Fc$^+$) +4.8 eV), where $E_{1/2}$ was obtained from the energy values of the CV spectrum using the following relation: $E_{1/2} = 1/2$ ($E_{pc} + E_{pa}$). The HOMO energy of the new HSM was sufficiently more positive than the valence band of the perovskite (−5.5 eV), indicating that the HSM is favorable for effectively extracting holes from the perovskite layer toward the counter electrode. From the relationship $E_{LUMO} = E_{HOMO} + E_g$, the LUMO energy was obtained, which was equal to −2.73 eV for diCNq-Aza and −2.17 eV for spiro-OMeTAD. Related data are listed in Table 1. Surprisingly, the LUMO energy level of diCNq-Aza was higher than the value of the perovskite conduction band, which is expected to effectively block the undesired electron back-transfer from the perovskite layer to the electrode.[26]

Herein, to achieve more negative formation energy (ΔG) to reach more stability, more attention is paid to reduce the LUMO energy level through the addition of an electron-withdrawing group (CN). The presence of the CN group in HSM leads to a red shift in the UV-vis peak and effectively reduces the LUMO energy level and has a significant effect on the performance of PSCs.

On the other hand, the lower LUMO energy enhances the energy alignment between the HSM and the perovskite layer. This improvement facilitates more efficient charge separation, blocks electrons, enhances hole extraction, and reduces recombination losses.[27,28] Consequently, the new SAML-HSM demonstrates greater electrochemical activity compared to the conventional spiro-OMeTAD, underscoring its suitability as an efficient HSM for PSCs. Furthermore, the ability to absorb light at longer wavelengths extends the absorption spectrum of the perovskite layer, enabling it to harness a broader spectrum of sunlight and potentially increase the light-harvesting efficiency.[29–33] Additionally, the T_g of the HSM is a critical parameter for the long-term stability of PSC devices. The Differential Scanning Calorimetry (DSC) curve for diCNq-Aza (Fig. 2c) shows a T_g of approximately 95.5 °C, which is comparable to that of spiro-OMeTAD (118.5 °C).[34,35] This similarity indicates that diCNq-Aza exhibits good thermal stability, confirming its suitability for use in stable PSCs. In particular, contact angle measurements confirmed that the hydrophobicity properties of the new SAML-HSM are comparable with the best HSM materials reported to date.[36,37] Measurements were made at $t = 0$, 3 seconds and 3 minutes from the water drop fall. The
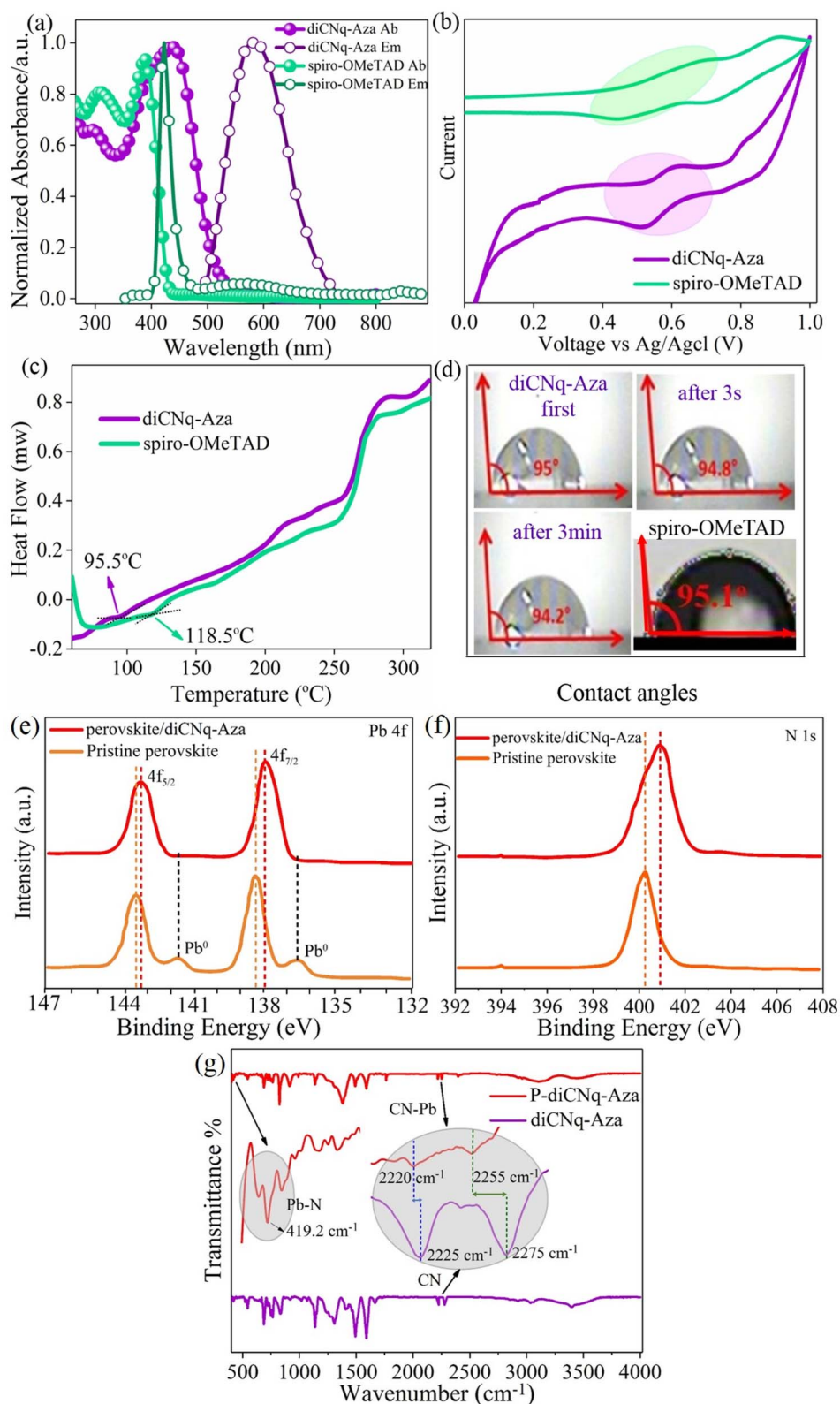
Fig. 2 Optical and electrochemical properties of the new HSM. (a) Normalized absorption (UV-vis) spectra (left) and luminescence (PL) spectra (right) of diCNq-Aza and spiro-OMeTAD in acetonitrile; (b) cyclic voltammograms of diCNq-Aza and spiro-OMeTAD in acetonitrile; (c) differential scanning calorimetry (DSC) curves of diCNq-Aza and spiro-OMeTAD (the value in the image is related to the glass transition temperature (T_g)); (d) the contact angles of diCNq-Aza and spiro-OMeTAD; (e) Pb 4f XPS spectra of perovskite films with and without diCNq-Aza passivation treatment; (f) N 1s XPS spectra of perovskite films with and without diCNq-Aza passivation treatment; (g) FTIR spectra of diCNq-Aza and P/diCNq-Aza films.

Table 1 The optical, electrochemical, thermal and hole mobility data for diCNq-Aza and spiro-OMeTAD

HTM/HSM	$\lambda_{\text{max.abs}}$[a] (nm)	$\lambda_{\text{max.em}}$[a] (nm)	λ_{int}[b]	E_g[c] (eV)	$E_{1/2}$[d] (eV)	E_{HOMO}[e] (eV)	E_{LUMO}[f] (eV)	T_g (°C)	η_{quench} (%)
diCNq-Aza	296 436	583	508	2.44	0.57	−5.17	−2.73	98.5	95
Spiro-OMeTAD	308 388	423	412	3.01	0.57	−5.18	−2.17	124.5	93

[a] UV-vis and photoluminescence spectra were measured in acetonitrile solution. [b] λ_{int} is the intersection point of normalized UV-vis absorption and emission curves. [c] Optical band gap was calculated from the formula: $E_g = 1240/\lambda_{\text{int}}$. [d] From CV measurements, $E_{1/2} = 1/2(E_{\text{pa}} + E_{\text{pc}})$. [e] $E_{\text{HOMO}} = -(E_{1/2} (\text{vs. Fc/Fc}^+) + 4.8 \text{ eV})$. [f] $E_{\text{LUMO}} = E_{\text{HOMO}} + E_g$.

results indicate that diCNq-Aza presents good hydrophobicity with a contact angle >90°, which is very close to the angle recorded for spiro-OMeTAD at $t = 0$ (Fig. 2d). Surprisingly, the water contact angle after 3 minutes had not changed and kept its shape in the most stable form on the new SAML-HSM.[38] This means that diCNq-Aza prevented water penetration into the perovskite surface after some minutes and thus did not destroy the perovskite immediately, which is promising for a stable SAML-HSM.

An important and effective factor in increasing the photovoltaic performance and long-term stability of perovskite solar cells is the diminishing of perovskite layer defects. To reduce defects and pin-holes, it is necessary to passivate the perovskite surface. In general, the empty 6p electron orbital of the unsaturated coordination Pb^{2+} ion in perovskite has a strong ability to form a coordinate covalent bond with Lewis bases.[39] As a result, the electron-donating atoms in Lewis base compounds can bind with Pb^{2+} eliminating the defects by deactivating the uncoordinated Pb^{2+} ions.[40] To investigate the molecular interactions between the perovskite layer and the new SAM, FTIR and X-ray photoelectron spectroscopy (XPS) techniques were used. The XPS spectra of the perovskite layers before and after passivation with diCNq-Aza were obtained and are presented in Fig. 2. As can be seen, Fig. 2e shows a high-resolution XPS spectrum of the Pb 4f orbitals, which shows that the binding energies of the two characteristic peaks Pb $4f_{7/2}$ and Pb $4f_{5/2}$ have shifted from 138.30 eV and 143.55 eV in the bare perovskite to lower binding energies of 137.95 eV and 143.25 eV in perovskite/diCNq-Aza, respectively. This shift confirms the interaction between the N atom of CN and Pb^{2+} and the formation of a C–N···Pb coordination bond. It is worth noting that two small peaks at 136.50 eV and 141.60 eV appear in the pure perovskite layer, which are related to metallic lead formed as a result of Pb^{2+} reduction. Metallic lead causes surface defects in the perovskite thin film and reduces the efficiency and stability of the PSC. In particular, as shown in Fig. 2e, the XPS peaks for metallic lead disappear in the XPS spectra of the perovskite thin films coated with diCNq-Aza. This confirms the coordination of CN with Pb^{2+} and the effective passivation of the defects in the perovskite thin film.[41,42] Subsequently, as observed in the high-resolution N 1s spectrum, the N 1s peak of the bare film was located at 400.28 eV and shifted to a higher binding energy by 400.89 eV after treatment with the new SAML (Fig. 2f). Full survey XPS spectra of perovskite films with and without diCNq-Aza passivation treatment were recorded and are presented in the ESI section, Fig. S1.†

Considering that the CN group has a stretching vibration peak at approximately 2200 cm^{-1} in the finger print region and as a result of binding to the metal, it shows a red shift due to the reduction of the cyanide bond order, further confirmation of the existence of the interaction between the CN group and Pb^{2+} can be provided by recording and comparing the FTIR spectra of diCNq-Aza before and after placement on the perovskite surface (Fig. 2g). The significant shift of the wavenumbers of the CN stretching vibration ($\nu_{\text{C}\equiv\text{N}}$) of diCNa-Aza to lower values after placement on perovskite from 2225 to 2220 cm^{-1} and from 2275 to 2255 cm^{-1} indicates the interaction between Pb^{2+} and the nitrogen atom of the CN group and bond formation. Furthermore, it is worth noting that a peak around 400–500 cm^{-1} can be attributed to Pb–N bonding, which is generally reported in the literature.[43] As displayed by the zoomed region of 400–500 cm^{-1}, the highlighted peak at 419 cm^{-1} is attributed to the formation of Pb–N bonding.

2.2 Hole mobility and SAML characteristics

The schematic structure and layer arrangement of a carbon-based perovskite solar cell (C-PSC) using diCNq-Aza as a new SAML-HSM is shown in Fig. 3a. Moreover, the energy-level diagram of diCNq-Aza in Fig. 3b shows that the estimated HOMO level of diCNq-Aza optimally matches with the valence band of the perovskite. In particular, the energy difference between the HOMO levels of the perovskite and diCNq-Aza ($\Delta\text{HOMO}_{\text{perovskite–diCNq-Aza}}$) is 0.33 eV, which produces the driving force necessary for hole transfer from perovskite to the HSM, confirming the better agreement between the interfacial charge extraction of new SAML-HSM/perovskite than the classic spiro-OMeTAD layers.

To investigate the hole extraction in more detail, we performed energy-dispersive X-ray (EDX) mapping on the perovskite passivated by the new SAML-HSM (Fig. 3c, left and S4†). The results clearly show good mixing between the diCNq-Aza species and the perovskite structure, indicating that the SAML-HSM effectively passivates the hole traps and defects in the perovskite layer by diffusing into it.

To validate these findings, scanning electron microscopy (SEM) images of bare perovskite films and those containing diCNq-Aza are shown in Fig. 3c (middle and right). The SEM images reveal a transition in surface morphology from spherical
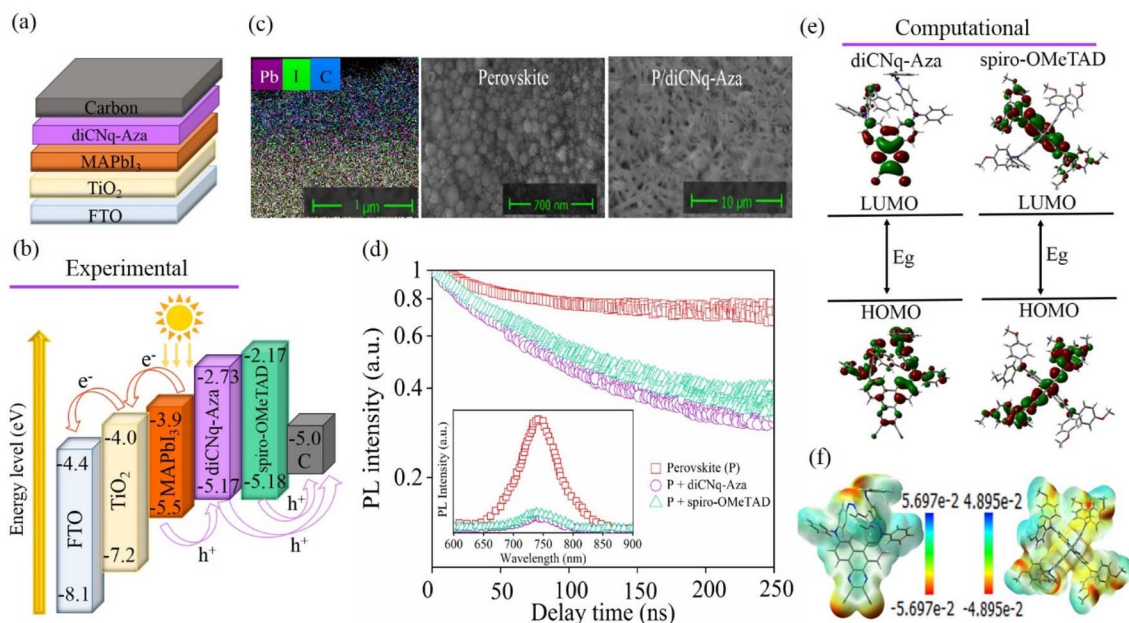
Fig. 3 (a) Schematic structure of a perovskite solar cell device using diCNq-Aza as the HSM; (b) the relative energy levels in the PSCs based on diCNq-Aza and spiro-OMeTAD; (c) EDX map and cross sectional (left) and top view SEM images of the perovskite and P/diCNq-Aza layers of the device (right); (d) the corresponding PL decay curves measured at a wavelength near the band gap that yields the maximum PL signal upon exciting the perovskite, perovskite/diCNq-Aza and perovskite/spiro-OMeTAD, and the inset plot is the steady-state PL spectra of the perovskite and p/HSM films; (e) DFT calculated frontier molecular orbital distributions and energies of the HOMO and LUMO levels for diCNq-Aza and spiro-OMeTAD. Red and green represent electrons and holes, respectively; (f) electrostatic surface potential (ESP) for the HSM, and regions of high and low potentials are indicated in red and blue, respectively.

to needle-like structures, corresponding to an increase in the degree of crystallization.

In this area, time-resolved photoluminescence (TRPL) was used to shed light on the carrier extraction process through quantitative approaches.[44,45] As shown in Fig. 3d, new SAML-diCNq-Aza quenches the PL of the perovskite more effectively than spiro-OMeTAD. The calculated PL quenching factor (η_{quench}) for diCNq-Aza (95%) is higher than that for spiro-OMeTAD (93%) (Table 1). Overall, PL measurements show that diCNq-Aza has more efficient hole extraction compared to spiro-OMeTAD.

To gain deeper insight into the electronic and geometric structures of diCNq-Aza, we applied the density functional theory (DFT) method with the Gaussian 09 program at the B3LYP/6–31 G level to optimize the ground-state geometry.[46] The optimized structures and energy levels of the frontier molecular orbitals for diCNq-Aza and spiro-OMeTAD are shown in Fig. 3e and S4.† Also, LUMO+1, LUMO, HOMO, HOMO−1, and HOMO−2 energy levels of diCNq-Aza and spiro-OMeTAD obtained from DFT calculations are shown in Fig. S6.†[47,48]

As is seen, the HOMO of diCNq-Aza is almost distributed over the electron donor moieties, while the LUMO is only localized on the anchoring groups, confirming the highest charge separation, which indicated that diCNq-Aza could be considered as an efficient D–A SAML-HSM in PSC. Furthermore, to gain a deep understanding of the charge distribution of diCNq-Aza and determine the appropriate groups that bind to the perovskite surface, we performed an electrostatic surface

potential (ESP) evaluation of the new SAML-HSM (Fig. 3f), which showed that the positive electrostatic potential is localized on the conjugated backbone. In contrast, the negative electrostatic potential corresponded to the strong electronegative ability of nitrogen atoms, which can serve as the Lewis base properties of the CN-anchoring group to passivate perovskite defects through the Pb atoms as a Lewis acid. In fact, remarkably, the ESP clearly indicated that CN groups are able to act as Lewis bases to coordinate with Pb atoms as the Lewis acid, confirming that diCNq-Aza could be considered as an SAML-HSM.

In the following, to investigate the charge transfer of diCNq-Aza, a thermally activated hopping model under room temperature conditions was used. According to the Einstein–Smolochovsky equation,[49] the hole mobility (μ) is given by:

$$\mu = \frac{e}{K_B T} D$$

where e is the elementary charge and D is the diffusion coefficient, which can be evaluated from the following equation:

$$D = \lim_{t \to \infty} \frac{1}{2d} \frac{\langle x(t)^2 \rangle}{t} \approx \frac{1}{2d} \sum_m r_m^2 K_m p_m$$

where d is the spatial dimensionality of the organic crystal ($d = 3$). $p_m = K_m / \sum_m K_m$ is the relative probability of a charge carrier to a particular mth neighbor. K_m is the hopping rate to the mth neighbor, which is obtained using the Marcus equation (refer to the ESI†), and r_m is the centroid-to-centroid distance to

Table 2 Calculated centroid-to-centroid distance (r_m), hole reorganization energy (λ_h), hole transfer integral (V_h), hole transfer rate (k_h), and hole mobility (μ_h) of diCNq-Aza and spiro-OMeTAD

| HTM/HSM	r_m (Å)	λ_h (eV)	V_h (eV)	k_h (s^{-1})	μ_h (cm^2 V^{-1} s^{-1})
diCNq-Aza	13.08	1.0204	0.0731	4.588×10^9	0.45×10^{-3}
Spiro-OMeTAD[52]	10.05	0.11	2.47×10^{-3}	3.77×10^{10}	2.47×10^{-3}

the neighbor m. The values of hole mobility (μ_h), centroid-to-centroid distances (r_m), hole transfer integral (V_h), and the hole transfer rate were calculated for the stable dimer of the diCNq-Aza. According to the data in Table 2, the diCNq-Aza shows a μ_h comparable to that of spiro-OMeTAD, and as a result, it works as an efficient HSM without extra doping.[50,51] Table S1 in the ESI† presents the calculated values of solubility in chlorobenzene, chemical hardness, and dipole moments of diCNq-Aza and spiro-OMeTAD.

2.3 Surface morphology

The surface morphology and roughness of the perovskite films with and without HSM were studied by atomic force microscopy (AFM).[53] As shown in the AFM topography, amplitude, and phase images in Fig. 4, diCNq-Aza formed smooth, homogeneous and pin-hole-free thin films.

The root mean square roughness (R_q) values of the perovskite surface reduce from 181 nm in perovskite bare to 4 nm in perovskite/diCNq-Aza, and the average roughness (R_a) likely reduces from 17 nm to 0.5 nm, suggesting the good film formation property of diCNq-Aza (which is important to prevent current leakage and facilitate better charge-collection efficiency in PSCs). In fact, good morphological properties with a low surface roughness of the new SAML-HSM in the solid thin-film form on a perovskite layer are desirable for hole extraction and transfer at the perovskite/SAML-HSM interface. Moreover, in
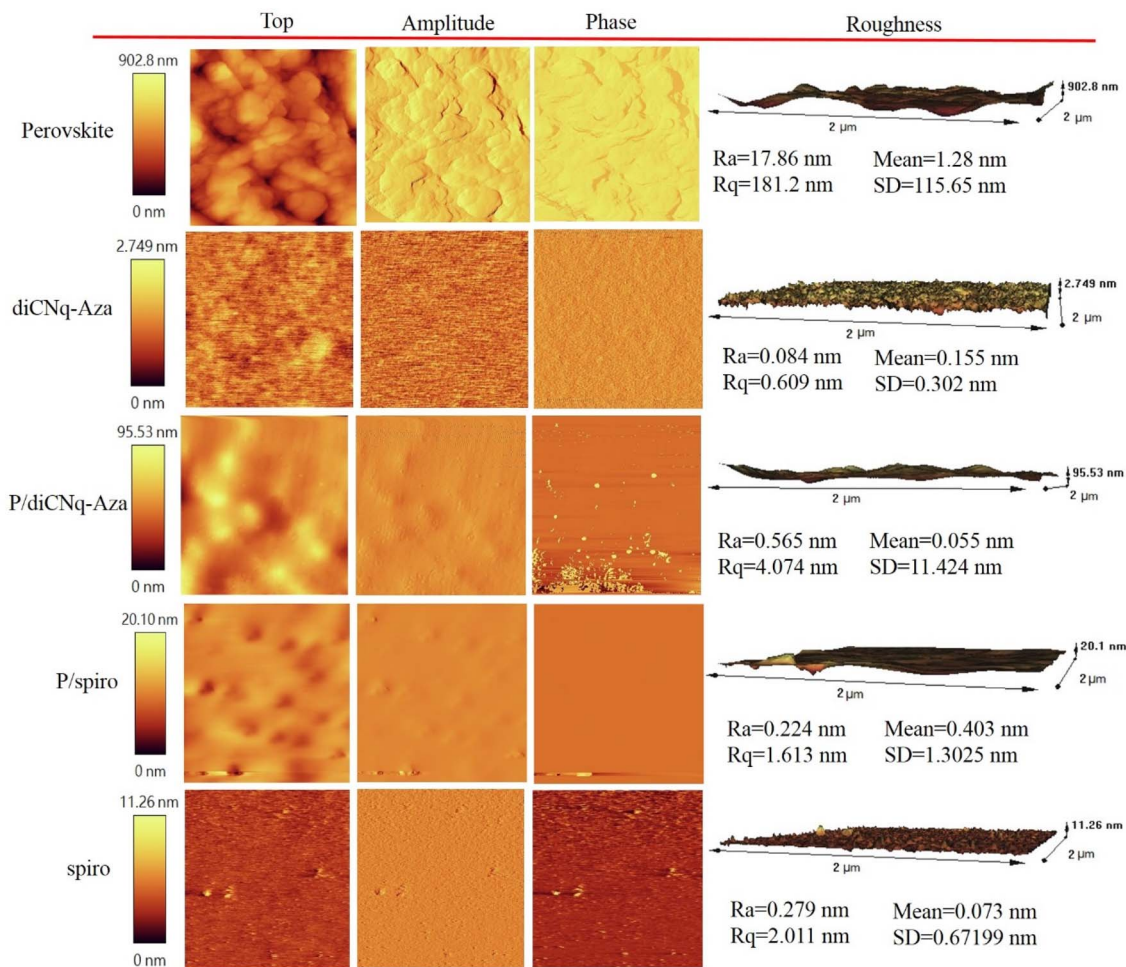
Fig. 4 AFM topography. AFM photos of bare perovskite, diCNq-Aza, perovskite/diCNq-Aza, perovskite/spiro-OMeTAD and spiro-OMeTAD. R_a is the average roughness, R_q is the root mean square roughness, and SD is the standard deviation of the profile heights.

Fig. 4, the bottom part, the relevant parameters for spiro-OMeTAD are shown for comparison with diCNq-Aza, and it can be seen that their values are close to each other.[54]

2.4 The absorption energy of the diCNq-Aza/CH₃NH₃PbI₃ system is based on VASP calculations

To explore the possible pathways of interaction of the new SAML-HSM with the perovskite layer, the diCNq-Aza/CH₃NH₃-PbI₃ system was geometrically optimized in Vienna *ab initio* simulation package (VASP) using projector-augmented wave methods with the PBE generalized gradient approximation (GGA) exchange correlation.[55,56] An energy cutoff of 400 eV was used, and the force convergence criterion for geometry optimization was set to 0.02 eV Å⁻¹. Herein, a perovskite supercell was prepared as the adsorption surface.

In order to determine the most stable coordination mode of CN groups of diCNq-Aza on the perovskite surface, three different types of possible connections (modes 1–3, Fig. 5 and S7†) were suggested, whose corresponding adsorption energy (E_{ads}) and the distance between the N atom in the diCNq-Aza and the Pb atom on the perovskite surface (d_{Pb-N}) were computationally optimized.

By considering the various coordination modes of CN groups with Pb atoms of the perovskite slab, surprisingly, our results indicated that the bidentate bridging mode (1) and monodentate mode (3) could efficiently bond to Pb atoms through the optimized bonding lengths of 2.67 Å and 2.70 Å, respectively,

which are less than the sum of *van der Waals radii* of Pb and CN atoms. These interesting results clearly indicated an important hypothesis that the CN group *via* the N atom forms a new bond with the Pb atom of the perovskite surface and fills the iodine vacancy after adsorption on the crystal structure surface to reduce trap states on the perovskite surface.[57]

The lone electron pairs on the N atom of diCNq-Aza can delocalize onto the 6p empty orbitals of Pb²⁺ to form coordination bonds with strong bonding strengths, while after optimizing mode (2), named bidentate chelation, the bonding length increased to 2.84 Å and 2.92 Å, which is rarely seen in the crystallographic literature.[58]

In the following, to find the most promising coordination mode based on the energy chemical absorption approach, the calculated E_{ads} values (from the following equation) for modes 1 and 3 were estimated at −1.04 eV and −1.12 eV, respectively, indicating the strong chemical adsorption of the new SAML-HSM onto the perovskite surface.

$$E_{ads} = E_{total} - E_{CH_3NH_3PbI_3} - E_{diCNq-Aza}$$

where E_{total}, $E_{CH_3NH_3PbI_3}$, $E_{diCNq-Aza}$ denote the energy of the diCNq-Aza/MAPbI₃ complex, MAPbI₃ and diCNq-Aza, respectively. In light of the above results, the amount of adsorption energy of mode (2) was calculated at about −0.122 eV, which is remarkably lower than those of modes 1 and 3. Therefore, the placement of diCNq-Aza on the perovskite in this mode is probably ruled out. It is also noteworthy that the number of
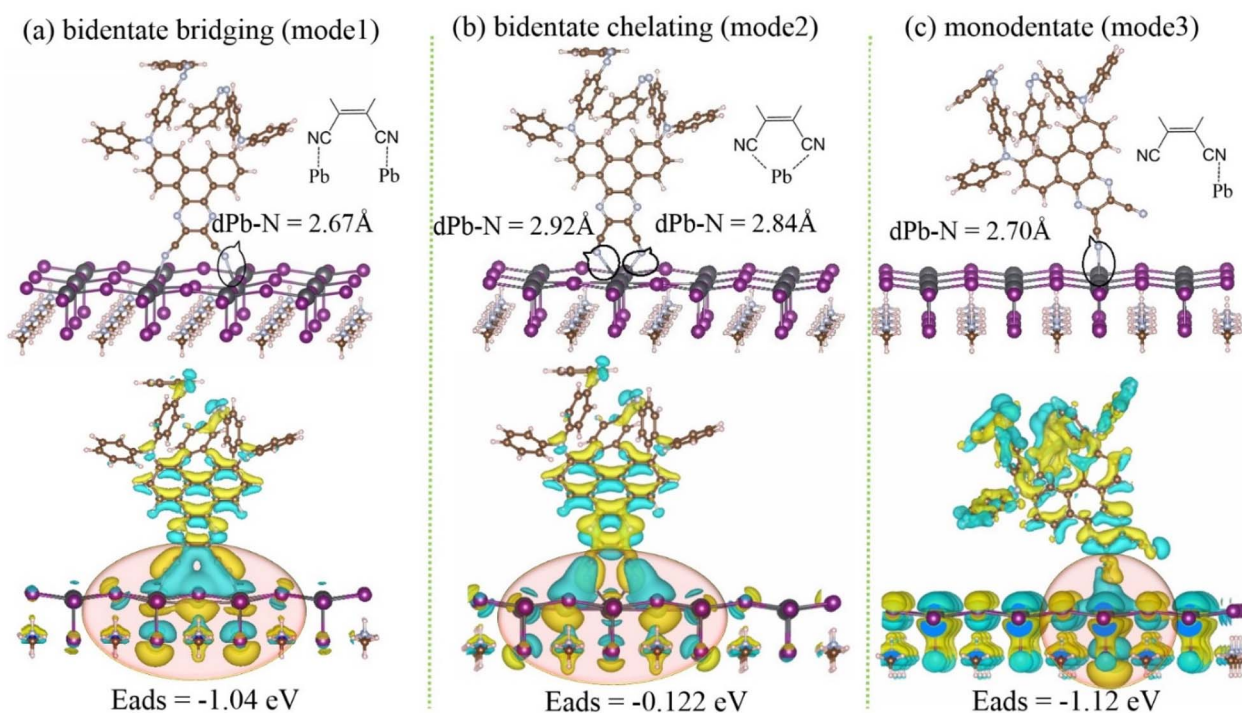
Fig. 5 Optimized structures. The optimized structures of possible binding modes of diCNq-Aza on the perovskite surface (up) and their charge density differences (CDD) (down) along with calculated adsorption energies (E_{ads}) are also shown. The yellow and blue regions represent charge accumulation and charge depletion in 3D space, respectively. The C, H, N, Pb, and I atoms are represented by brown, pink, blue, dark gray, and purple spheres, respectively.

optimization cycles of mode (1) is about half of mode (2) (47 and 87 cycles, respectively), which proves the earlier evidence. Obviously, herein, the results clearly indicated that the newly molecular synthesized HSM could efficiently act as an SAML through the coordination of its two CN groups onto the surface of perovskite *via* one nitrogen atom of the CN group to one Pb atom of perovskite, namely bidentate bridging (mode 1).

The simulated charge transfer from the HSM to the perovskite, assessed in three different coordination modes, clearly demonstrates that varying these modes alters the amount of charge transfer. This observation confirms the strength of the interface interaction between the new HSM and the perovskite surface, as illustrated in Fig. 5, where the size of the circles highlights this relationship. As detailed in the figure, the
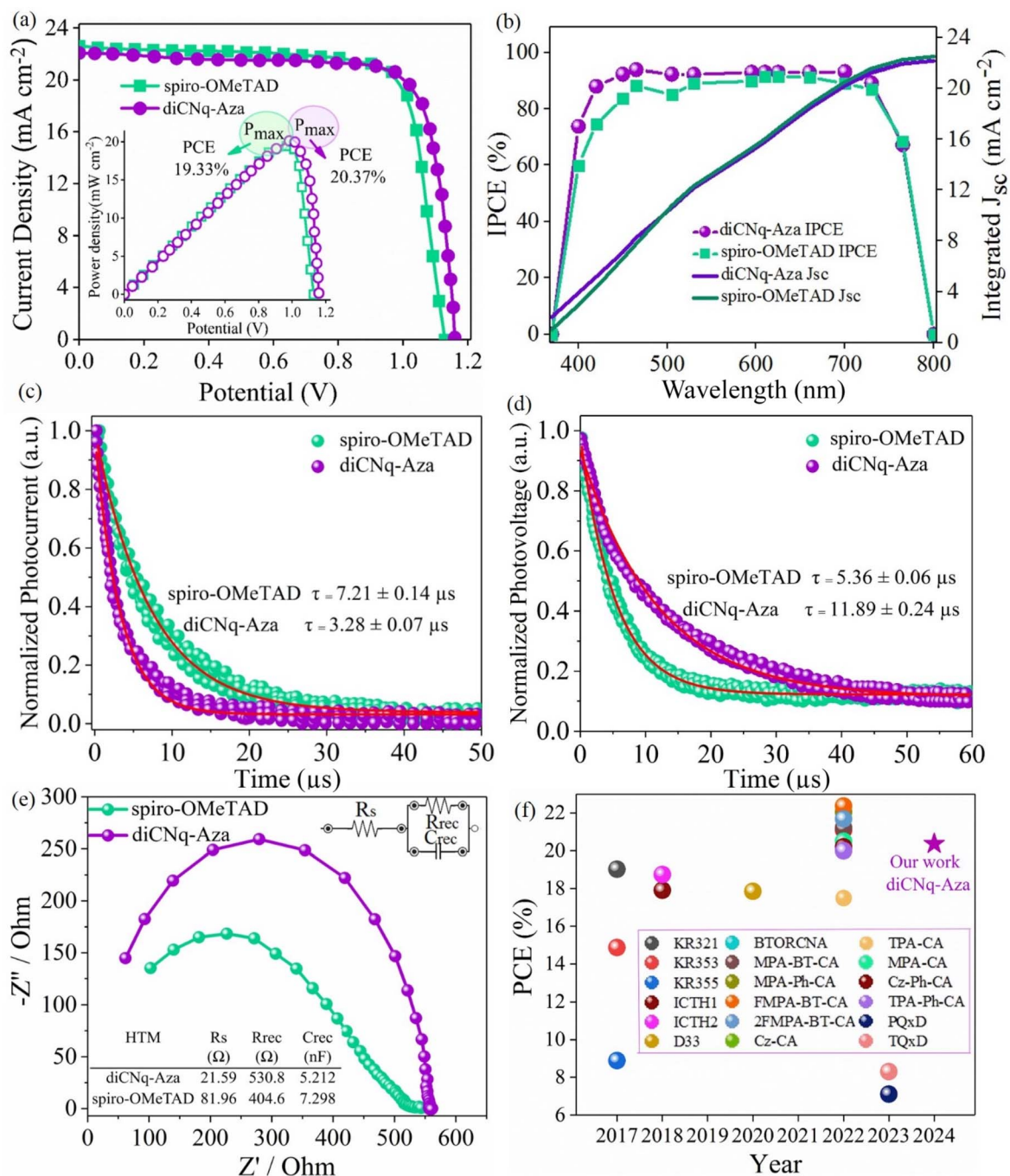
Fig. 6 Photovoltaic performances of the FTO/TiO$_2$/MAPbI$_3$/HSM/C system. (a) *J–V* curves of the best-performing devices based on diCNq-Aza and spiro-OMeTAD (inset plot is the power density–voltage curve for these HSM-based systems); (b) IPCE spectra and integrated current curves of the corresponding devices; (c) the TPC curves and (d) the TPV curves of diCNq-Aza- and spiro-OMeTAD-based devices, respectively; (e) Nyquist plot (impedance spectra) and equivalent circuit for the film of perovskite with HSMs; (f) comparison between PCEs for PSCs with SAML-HSMs reported in relevant literature from 2017 to 2024 (the molecular structure of SAML-HSMs and the photovoltaic data are given in the ESI, Table S4, Fig. S10†).

highest charge transfer occurs in the bidentate bridging mode (mode 1), followed by the bidentate chelating mode (mode 2), and ultimately the monodentate mode (mode 3).[59]

2.5 Photovoltaic performance

For evaluation of the device performance of HSMs, the photocurrent density–voltage (J–V) characteristics of control and target devices (FTO/TiO$_2$/MAPbI$_3$/HSM/C) were investigated under AM 1.5 G irradiation at 100 mW cm^{-2}, and the current density–voltage (J–V) curves are shown in Fig. 6a. The obtained parameters are summarized in Table 3.[60]

The photovoltaic performance of the new SAML-HSM showed a better PCE value than the benchmark spiro-OMeTAD through an open-circuit voltage (V_{OC}) of 1.16 V,[61] a short circuit current density (J_{SC}) of 22.27 mA cm^{-2} and a fill factor (FF) of 0.79, resulting in a PCE of 20.37% (the PCE mean value is 19.83%), while, under the same conditions, the PSC based on spiro-OMETAD PCE decreases to 19.33% (with the PCE mean value of 18.65%). To the best of our knowledge, the obtained PCE of 20.37% is amongst the best values of PSC based on the carbon cathode, which has been reported so far. Radiative recombination due to the favored passivation of the perovskite surface by CN groups results in more efficient hole extraction by the new SAML-HSM than the classic spiro-OMeTAD. Moreover, as earlier shown based on XPS, FTIR and computational studies, the anchoring groups of diCNq-Aza coordinated into the surface of perovskite via the Pb atom, which stabilized the composite of diCNq-Aza/perovskite.

Given that the carbon electrode functions as an HSM, the new SAML-HSM was evaluated in a PSC incorporating a metal electrode. This assessment confirmed efficient hole mobility from the perovskite layer to the metal electrode. Notably, the carbon-PSC utilizing the new SAML-HSM exhibited only about 2% lower efficiency than the gold-PSC based on spiro-OMeTAD, indicating strong compatibility of the new diCN-HSM with the carbon electrode (data provided in Fig. S8 in the ESI†).

Fig. 6b illustrates the external quantum efficiency (EQE) curves for the devices based on the new SAML-HSM and classic spiro-OMeTAD, for which the integrated current density values (J_{SC}), calculated from the integration of the incident photon-to-electron conversion efficiency (IPCE) spectra, were 21.58 mA cm^{-2} and 22.48 mA cm^{-2}, respectively, which are almost in agreement with the values obtained from the J–V curves. The higher IPCE value of the device containing diCNq-Aza (93.24%) than the device with spiro-OMeTAD (86.41%) in the broad range of 400–750 nm suggest better charge carrier separation and hole

extraction ability in the new SAML-HSM. The PCE distribution and static data for 24 cells of diCNq-Aza and spiro-OMeTAD devices exhibited a narrow range, which is comparable with silicon solar cells,[61] as shown in Fig. S9.†

We have used the transient photocurrent (TPC) and the transient photovoltage (TPV) techniques to investigate the mechanisms of charge extraction and non-radiative recombination in the novel SAM-based perovskite solar cells. The TPC technique, which measures the change in the photocurrent passing through the device, is related to the measurement of charge carrier transport, and the TPV technique is related to the charge carrier recombination.[62] The charge carrier extraction was determined using a single exponential fit to the TPC curves, and the device lifetime was determined using a double exponential fit to the TPV curves. The fitting results are listed in Table S2.†[63,64] As can be seen from Fig. 6c and d, the cell with diCNq-Aza exhibits faster decay and a shorter charge extraction time ($\tau = 3.28$ μs) compared to the spiro-OMeTAD ($\tau = 7.21$ μs) containing cell, confirming the more efficient extraction of charge carriers in this cell. Surprisingly, the new SAM-based device has a longer carrier lifetime at 11.89 μs compared to 5.36 μs for the control device, indicating better suppression of non-radiative recombination.

To gain deeper insight into the interfacial charge transfer and recombination processes at the perovskite/HSM interface, we conducted electrochemical impedance spectroscopy (EIS) measurements on PSCs. The Nyquist plot and the corresponding equivalent circuit are presented in Fig. 6e, with detailed data provided in Table S3.† Each circuit features a series resistance (R_s) attributed to the contact resistance of the electrical wire and fluorine-doped tin oxide (FTO) electrode, which can be determined from the high-frequency intercept on the real axis. Notably, the new self-assembled monolayer HSM diCNq-Aza exhibits a low R_s of 21.59 Ω, indicating effective passivation of perovskite surface defects and optimal interfacial contact, contributing to an increased FF, as observed in the photovoltaic performance. Additionally, the arc diameter in the Nyquist plot, which can be accurately fitted using the equivalent circuit, is indicative of the recombination process and consists of two components: recombination chemical capacitance (C_{rec}) and recombination resistance (R_{rec}). The higher R_{rec} value of 530.8 Ω for diCNq-Aza versus spiro-OMeTAD (404.6 Ω) signifies reduced recombination and enhanced charge transport, attributed to improved film quality and fewer defects, resulting in higher V_{OC} and FF.[65,66] To provide a clear overview of the photovoltaic performance of the new SAML-HSM, Fig. 6f and Table S4† present a historical comparison of PCEs for PSCs with various SAML-HSMs containing CN and CNCOOH groups, as reported in the literature from 2017 to 2024 (ref. 58 and 67–73) (molecular structures are shown in Fig. S10†). The highest PCE values reported for these PSCs, using metal cathode electrodes, range from 22% to 23%. Surprisingly, the PCE of the diCNq-Aza SAML-HSM reached 20.37% when using carbon electrodes, which is competitive with metal cathode-based devices. Notably, the literature on PSCs with HSMs and carbon electrodes is limited, as C-PSCs typically function without HSMs. This underscores the potential of CPSCs based on SAML-HSMs as promising

Table 3 Photovoltaic parameters of PSCs (FTO/TiO$_2$/MAPbI$_3$/HSM/C) based on diCNq-Aza and spiro-OMeTAD

HTM/HSM	J_{SC} (mA cm^{-2})	V_{OC} (V)	FF (%)	PCE (%)
diCNq-Aza	22.27	1.16	78.85	20.37 (19.83)[a]
spiro-OMeTAD	22.60	1.13	75.69	19.33 (18.65)[a]

[a] Average PCE for 24 cells.

alternatives to metal-based PSCs, particularly those with gold cathodes. This work reports the first efficient PSC based on SAML-HSMs containing CN groups as anchoring sites, achieving a PCE greater than 20%.

2.6 Device stability

Lastly, the stability of our CPSCs based on the new SAML is preliminarily evaluated through thermal aging and shelf-life aging, showing satisfactory performance even without
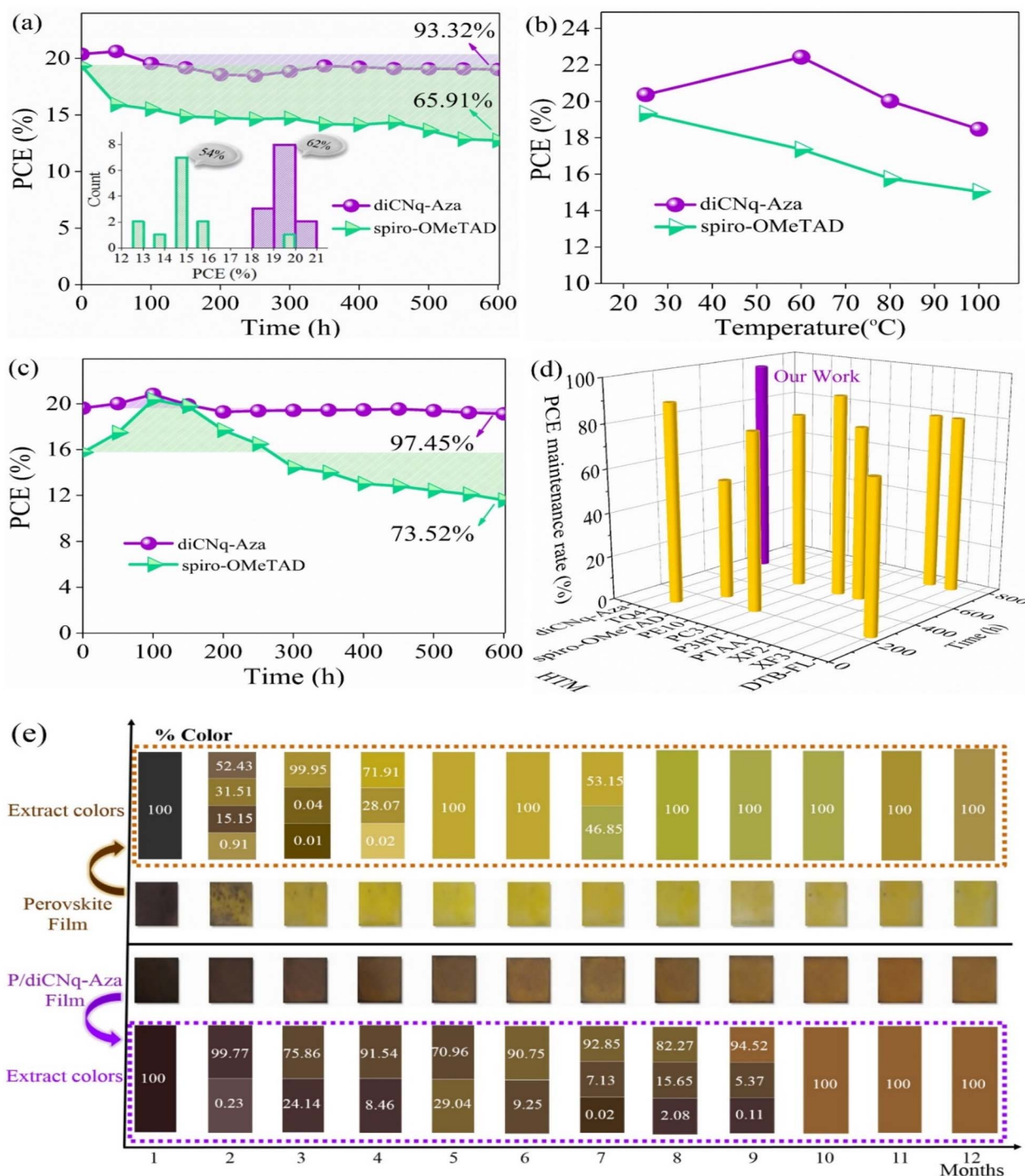

Fig. 7 Stability measurements and aging test results of PSCs (FTO/TiO$_2$/MAPbI$_3$/HSM/C) containing HSMs. (a) Long-term photostability of diCNq-Aza- and spiro-OMeTAD-based PSCs at 25 °C (the inset plot is a column chart of multiple times with the same PCE%); (b) the PCE changes at 4 incremental temperatures; (c) long-term thermal stability at 80 °C; (d) PCE maintenance rate (%) in PSCs based on different HSM-based literature; (e) stability test photos of fresh and aged films at regular intervals under ambient conditions with a temperature of 25 °C for one year. Up: films and color bars of perovskite; down: films and color bars of perovskite with diCNq-Aza. The colors are extracted from the images, and the numbers written in the color bars show the percentage of different colors in the films.

encapsulation. To shed light on the photostability behavior of new diCNq-Aza as the SAML-HSM, the long-term stability at room temperature was tested. Photocurrent–voltage (*J*–*V*) characteristics of the devices were measured under standard conditions under simulated AM 1.5G sunlight. As can be seen in Fig. 7a, the efficiency of the new SAML-HSM retains the maximum value of 20.61 in the first 50 hours, and in the next 200 hours, we see a slow decline, which increases again in the following hours, and finally, after 600 h of aging, the PCE still retained 93.32% (19.01) of its initial PCE value. Surprisingly, the PCE values of PSCs based on classic spiro-OMeTAD dramatically decreased within the first 50 h, which continued by about 400 hours, and finally, a drop of the PCE to 65.91% (12.74) of the initial value was observed at the end of 600 hours. In fact, as clearly shown in Fig. 7a, based on the highlighted sub-area schematic, which defines the loss of PCE over time, the newly designed SAML-HSM indicated a much lower PCE loss than spiro-OMeTAD, indicating excellent photostability of diCNq-Aza over time. The inset plot of Fig. 7a confirms that about 400 hours (60%) of total left time under illumination, the PCE of the new HSM was maintained in the range of 19–19.5%, while the spiro-OMeTAD indicates efficiency in the range of 14.5–15% for about 50% of the duration time. Statistical stability data of J_{SC}, V_{OC}, FF, and PCE for the PSCs based on diCNq-Aza and spiro-MeOTAD are collected in Table S5.†

Further investigations were conducted to assess the thermal stability of the device over a range of temperatures from 25 °C to 100 °C, aiming to understand the effects of temperature combined with illumination on system stability (Fig. 7b). With the exception of 60 °C, both devices exhibited similar performance trends at other temperatures. Notably, when the PSC based on diCNq-Aza was maintained at 60 °C, the PCE increased to 22.42%, representing approximately a 10% improvement compared to the same PSC at 25 °C. This suggests that elevated temperatures can effectively enhance the PCE over time. Higher temperatures positively impact PCE by improving the crystallinity of the perovskite, thereby enhancing the charge mobility and facilitating more efficient hole extraction.[74–77]

Fig. 7c displays the thermal stability of the new self-assembled monolayer HSM at 80 °C, with diCNq-Aza showing a PCE of 19.62%, while spiro-OMeTAD exhibited a decline to 15.75%. Notably, after 100 hours at this temperature, the maximum PCE values for both HSMs reached approximately 20.82% for diCNq-Aza and 20.35% for spiro-OMeTAD. Interestingly, the PCE values increased by about 6% and 29% from their initial readings for diCNq-Aza and spiro-OMeTAD, respectively. During the subsequent 100 hours, diCNq-Aza maintained the PCE close to its original value, demonstrating stable performance, ultimately showing 97.45% of its initial efficiency at 600 hours. In contrast, the spiro-OMeTAD system exhibited marked fluctuations in efficiency between 100 and 600 hours, experiencing a rapid decline after reaching its maximum PCE and ending at 73.52% of its initial efficiency. To our knowledge, this thermal stability behavior is among the best documented for organic HSM-based PSCs to date. For additional photovoltaic data related to temperature stability at 80 °C, please refer to Table S6.†

The photo and thermal stability of PSCs based on diCNq-Aza significantly exceed those of spiro-OMeTAD. This enhanced stability can be attributed to the strong Pb–N interactions between the SAML-HSM and the perovskite, which effectively passivate defects within the perovskite layer. These results underscore the essential role of diCNq-Aza in protecting the perovskite device from degradation. Fig. 7d illustrates that the new SAML featuring a C–N anchoring group exhibits the highest thermal stability over time at 80 °C compared to other SAML families, with additional details of the molecular structures summarized in Table S7.†

2.6.1 One-year photographic stability. The stability of an HSM is a critical factor for industrialization and commercialization. In this study, the photostability of the thin film of the new SAML-HSM applied to the perovskite layer was monitored for one year under ambient conditions without encapsulation (see Fig. S11†).

Fig. 7e displays images of PSC films, illustrating color changes over time. This straightforward and effective stability test involves monitoring the transition between two contrasting colors: dark brown, representing the perovskite, and yellow, denoting the decomposed perovskite. The color analysis was conducted using "Extract Colors from Image" software, where the extracted colors correlate to the year-long study, with the numbers on the color bars indicating the percentage of each color present in the films. As shown in Fig. 7e, the unprotected perovskite film began to change from dark brown to yellow within two months of light exposure, indicating degradation into PbI_2. In contrast, the color change in the diCNq-Aza-containing perovskite film was minimal; after two months, this film exhibited nearly 100% retention of its original color. The compositional images of the aging perovskite combined with the new SAML indicate that approximately 90% of the original color was retained after nine months, confirming the remarkable stability of the diCNq-Aza SAML-HSM perovskite interface over an extended period.

2.7 Estimating the cost of producing a new HSM and comparing it with other HTM/HSMs

An important advantage of the new SAML-HSM compared with spiro-OMeTAD is the much lower synthesis cost. The synthesis cost of 1 gram diCNq-Aza was estimated according to the cost models of Petrus *et al.*[78] and Osedach *et al.*[81] and compared with the price of 1 gram spiro-OMeTAD. The prices of the materials used were obtained from Sigma-Aldrich. In summary, the estimated cost of diCNq-Aza is 27.5 \$ per g (Table S8†) which is a 10-fold reduction compared to the cost of spiro-OMeTAD (27.3 \$ per g).[79,80] In addition, to compare the price of the new SAML-HSM with spiro-OMeTAD at different PCEs of corresponding PSCs, the cost per peak watt was calculated using the following equation,[81] where η is the solar cell efficiency (PCE%) in the range of 2–30%, C_g is the cost per gram, ρ is the density, which is assumed to be 1.1 g cm^{-3}, t is the thickness of the donor material, which is assumed to be 100 nm and I is the solar irradiance under peak conditions, which is assumed to be 1000 W m^{-2}.
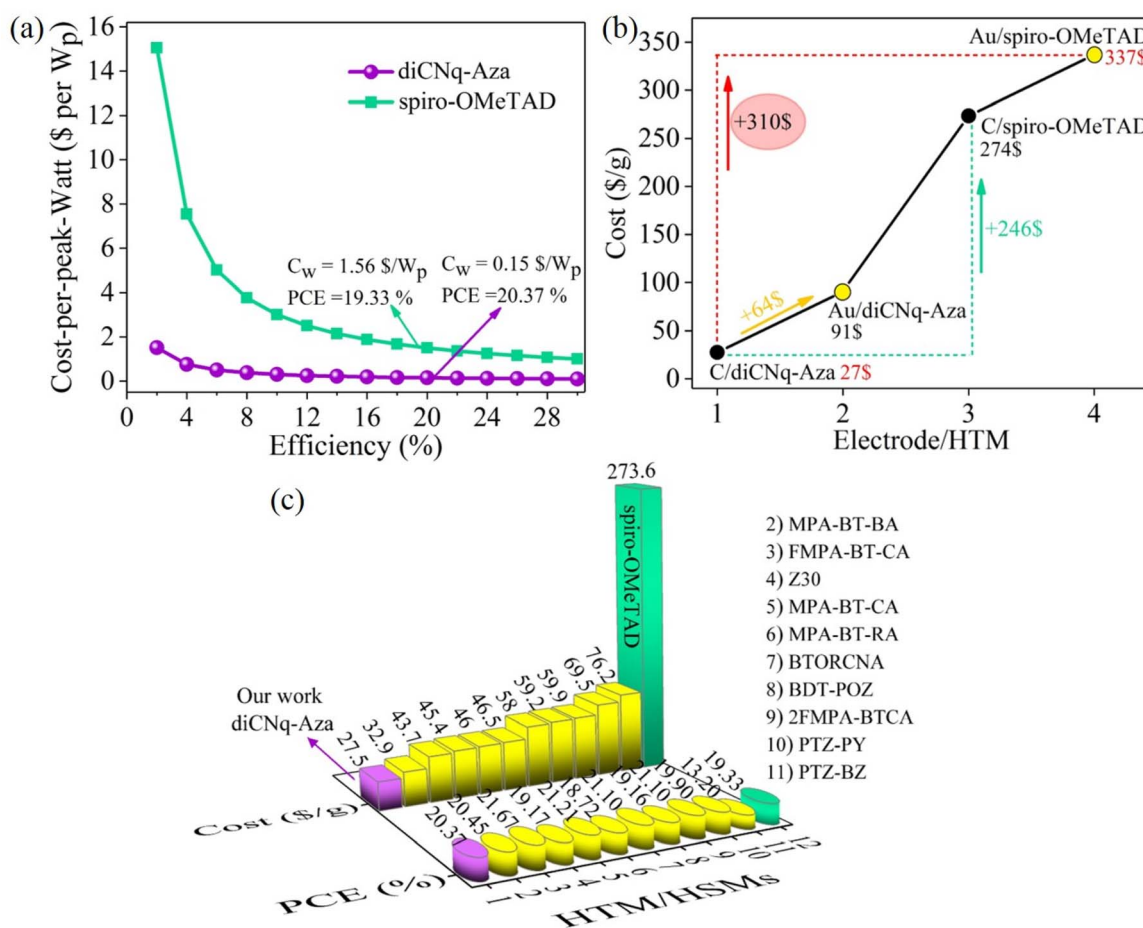
Fig. 8 Cost estimates. (a) Cost per peak watt ($ per W_p) for diCNq-Aza and spiro-OMeTAD; (b) graph of changes and comparison of costs in gram for PSCs with carbon or gold as the electrode and diCNq-Aza or spiro-OMeTAD as the HTM/HSMs; (c) comparison between costs and PCEs of PSCs with different HTM/HSMs, as reported in our work and other relevant studies. The HTM/HSMs are named with numbers from 1 to 12. Their full names are listed in a column next to the chart.

$$C_w = \frac{C_g \times \rho \times t}{\eta \times I}$$

According to Fig. 8a, C_w as a function of PCE, shows that the cost of preparing diCNq-Aza is much more economical than spiro-OMeTAD. The values mentioned inside the graph are the cost per watt peak in the PCEs obtained for HTM/HSMs in this study (Photovoltaic performance section), where the cost value at PCE = 20.37% is equal to 0.15 $ per W_p, which is more than ten times lower compared to 1.56 $ per W_p for spiro-OMeTAD at PCE = 19.33%.

In particular, given that the type of cathode electrode used also has a significant impact on the cost of a solar cell, a comparison was made between the price of the conventional gold electrode and the carbon electrode used in this study. Specifically, carbon paste costs between €10 and €100 per kg, and 20 g m^{-2} is required to deposit a 20 μm carbon film. This results in a final cost of approximately €0.20 to €2.00 per m^2 for the carbon electrode. In contrast, the cost of a gold electrode, assuming a thickness of 100 nm, at the current gold price of €55 to €60 per gram, ranges from €1062 to €1159 per

m^2. Fig. 8b shows the graph of the cost changes in grams for producing one gram of the new SAML-HSM and one gram of spiro-OMeTAD in PSCs with two different types of carbon and gold electrodes. Since other cell components are constant in all the desired PSCs, their costs are not included, and the reported costs are the sum of the price of one gram of electrode and one gram of HTM/HSM. Four different compounds of two types of electrodes (carbon and gold) and two different HTM/HSMs were systematically compared, C/diCNq-Aza, Au/diCNq-Aza, C/spiro-OMeTAD and Au/spiro-OMeTAD. The expected cost values for these four combinations are 27.51, 90.75, 273.61 and 336.85 $ per gram, respectively, and are shown in Fig. 8b. As can be seen, changing the electrode from carbon to gold and keeping the HSM constant result in a cost increase of more than 63 $, as well as when the carbon electrode is fixed and the HSM changed from diCNq-Aza to spiro-OMeTAD, an increase of about 246 $ was observed. The significant difference in cost is when the carbon electrode is replaced with the gold electrode and the new SAML-HSM with spiro-OMeTAD, it result in a cost increase of about 310 $. This large difference in price definitely justifies and proves the economic viability of

the proposed cell based on the carbon cathode and new molecule.

In addition to spiro-OMeTAD, other small organic HTM/HSMs can be compared to diCNq-Aza in terms of synthesis cost and PCE of the corresponding cells (Fig. 8c). In a short comparison between the newly proposed HSM and ten other HTMs mentioned in previous studies, the new HSM had the lowest production cost in dollars per gram, with a PCE almost equivalent to the highest PCEs reported so far.

3. Conclusion

The newly designed diCNq-Aza, as an SAML-HSM, demonstrates significant potential for efficient carbon electrode PSCs. The functional CN group, conjugated with π-extended Aza units, acts as an effective anchoring group that binds to the perovskite surface. Our results show that the SAML-HSM layer facilitated the formation of a uniform perovskite nanocrystal layer with excellent crystallinity, morphology, and minimal roughness. The interaction between the CN group and Pb^{2+} ions reduces surface defect densities and minimizes energetic mismatches between the perovskite and HSM. Based on the calculated absorption energies for different connection modes, we identified the bidentate bridging configuration (mode 1) as the most stable and favorable. Notably, the PSC utilizing the carbon electrode achieved a PCE of 20.37%, surpassing that of spiro-OMeTAD-based devices and ranking among the highest reported values for carbon-based PSCs. Moreover, the photo-thermal stability of the PSC with the new SAML-HSM retained over 95% of its initial performance at 80 °C, demonstrating exceptional thermal resilience for carbon-based PSCs. Remarkably, after nearly one year, the PSC exhibited no visible degradation, whereas the unmodified perovskite collapsed within one month. Our findings pave the way for market-competitive carbon-based PSCs by integrating the new C–N functionalized SAML-HSM with carbon electrodes.

Moreover, the cost-effective PSC utilizing the diCNq-Aza SAML-HSM with a carbon cathode reduces the overall production costs while facilitating easier layer deposition, thereby achieving three key benefits: (1) high efficiency (over 20% PCE), (2) high stability (more than 90% retention), and (3) low cost. Substantial cost difference highlights the significant economic advantage of using carbon-based electrodes in PSCs, particularly for large-scale production where cost efficiency is essential.

4. Experimental

4.1 Synthetic procedures of the target HSM

diCNq-Aza was successfully synthesized *via* two simple steps and was purified by recrystallization and column chromatography. The molecular structures and synthetic routes are shown in Fig. 1. diCNq-Aza was thoroughly characterized by FT-IR, ^{1}H-NMR, and ^{13}C-NMR spectroscopy, and the obtained results were found to be consistent with the proposed molecular structure.

4.2 Synthesis of 7,10-dibromobenzo[*f,h*]quinoxaline-2,3-dicarbonitrile (3 in Fig. 1)

At first, 0.22 g (0.6 mmol) of (3,6-dibromophenanthrene-9,10-dione) (**1** in Fig. 1) and 0.064 g (0.6 mmol) of 2,3-diaminomaleonitrile (**2** in Fig. 1) were weighed and poured into a 25 ml flask and then 10 ml of acetic acid was added to them. The resulting mixture was refluxed for 8 hours under a nitrogen atmosphere at a temperature of 127 °C. After cooling down to ambient temperature, the reaction product was added to cold distilled water, and the precipitate was filtered and washed with distilled water several times (~91% yield). ^{1}H-NMR (250 MHz, CDCl$_3$); δ = 9.04 (d, 2H); 8.7 (d, 2H); 7.96 (dd, 2H). CHN: anal. calcd. For $C_{18}H_6Br_2N_4$ (%): C, 49.352; H, 1.383; Br, 36.475, N, 12.79, ESI-MS: m/z, 434.721, [M–H]$^+$.

4.3 Synthesis of 7,10-bis(phenyl(4-((*E*)-phenyldiazenyl) phenyl)amino)dibenzo[*f,h*]quinoxaline-2,3-dicarbonitrile (diCNq-Aza)

A mixture of CuI (0.050 g), 1,10-phenanthroline (0.10 g), Cs$_2$CO$_3$ (2.00 g), **3** in Fig. 1 (0.44 g, 1 mmol), 4-(phenylazo)diphenylamine (**4** in Fig. 1) (0.546 g, 2 mmol) and 5 ml of dimethylformamide (DMF) was heated under reflux for 72 h under a nitrogen atmosphere at a temperature of 150 °C. After cooling to ambient temperature, the product was extracted by using CH$_2$Cl$_2$ and H$_2$O. The combined organic phases were dried over anhydrous MgSO$_4$ and evaporated (85% yield). ^{1}H-NMR (250 MHz, CDCl$_3$); δ = 6.9–7.15 (m, 6H), 7.19 7.32 (m, 10H), 7.47–7.50 (m, 6H), 7.76–7.90 (m, 8H), 8.26 (d, 2H), 8.82 (d, 2H). CHN: anal. calcd. For $C_{54}H_{34}N_{10}$ (%): C, 78.813; H, 4.166; N, 17.027. ESI-MS: m/z, 821.29, [M–H]$^+$.

4.4 Fabrication of PSCs

First, small glass slices coated with fluorine-doped tin oxide (FTO) were etched with zinc powder and 2 M HCl in deionized water to be used as substrates for making solar cells. Then, the substrates were cleaned with detergents and deionized water and were washed in 4 stages, respectively, with deionized water, 0.1 M HCl solution in ethanol, acetone, and ethanol, using ultrasonic waves. Next, on these substrates, mesoporous TiO$_2$ layers (150–200 nm) were deposited by spin coating TiO$_2$ paste diluted with absolute ethanol in a volume ratio of 1 : 8 at 2000 rpm for 10 seconds. To prepare MAPbI$_3$, 460 mg of lead(II) iodide (PbI$_2$) and 300 mg of methyl ammonium iodide (MAI) were added separately in 1 ml of *N,N*-dimethylformamide (DMF) and isopropanol alcohol, respectively. Then, the PbI$_2$ solution was spin-coated at 3200 rpm for 20 s on the mesoporous TiO$_2$ layers. The samples were annealed at 100 °C for 10 min. After cooling, the MAI solution was spin-coated on the PbI$_2$ films at 3200 rpm for 20 s. Finally, the MAPbI$_3$ layers were heated at 100 °C for 10 min. The substrates were then annealed at 100 °C for 1 h on a hot plate. The HSM solution was prepared by dissolving the HSMs in chlorobenzene. Then, 18 ml LiTFSI (from a stock solution in acetonitrile with a concentration of 1.0 M) and 29 ml *tert*-butyl pyridine (from a stock solution in chlorobenzene with a concentration of 1.0 M) were added to the

spiro-OMeTAD solution. The HSM was applied onto the perovskite film through spin coating the HSM solutions at a speed of 4000 rpm for 20 s. Subsequently, the substrates were dried at 100 °C for 5 min.[82] Finally, the C cathode was deposited by doctor-blading the corresponding pastes, which were then dried at 100 °C for 30 min.[83]

Data availability

Supporting data are included in the article's ESI.†

Conflicts of interest

There are no conflicts to declare.

Abbreviations

SAML	Self-assembled molecular layer
HSM	Hole-selective material
PSC	Perovskite solar cell
PCE	Power conversion efficiency
VASP	Vienna ab $initio$ simulation package
E_{ads}	Adsorption energy
Spiro-OMeTAD	2,2′,7,7′-Tetrakis (N,N-di-p-methoxyphenylamine)-9,9′-spirobifluorene
ISOS-D-1	Thermal aging and shelf-life aging
HTM	Hole transport material
HSM	Hole-selective materials
FF	Fill factor
V_{OC}	Open-circuit voltage
PA	Phosphonic acid
CA	Carboxylic acid
CAA	Cyanoacetic acid
ESI	Electronic Supplementary Information†
D–π–A	Donor–π–acceptor
diCNq-Aza	7,10-Bis(phenyl(4-((E)-phenyldiazenyl)phenyl)amino)dibenzo[f,h]quinoxaline-2,3-dicarbonitrile
SAML-HSM	SAML-type HSM
LITFSI	Lithium bis(trifluoromethanesulfonyl)imide
Cs_2CO_3	Cesium carbonate
CuI	Copper iodide
UV-Vis	Ultraviolet-visible
PL	Photoluminescence
λ_{max}	Maximum wavelength
E_g	Optical band gap
em	Emission
E_{LUMO}	Lowest unoccupied molecular orbital energy
CV	Cyclic voltammetry
E_{HOMO}	Highest occupied molecular orbital energy
ΔG	Formation energy
T_g	Glass transition temperature
DSC	Differential Scanning Calorimetry
C-PSC	Carbon-based perovskite solar cell
EDX	Energy-dispersive X-ray
SEM	Scanning electron microscopy
TRPL	Time-resolved photoluminescence
η_{quench}	PL quenching factor
DFT	Density functional theory
VB	Valence band
CB	Conduction band
ESP	Electrostatic surface potential
μ_h	Hole mobility
AFM	Atomic force microscopy
R_q	Root mean square roughness
R_a	Average roughness
SD	Standard deviation of the profile height
GGA	Generalized gradient approximation
$MAPbI_3$ ($CH_3NH_3PbI_3$)	Methyl ammonium lead iodide
FTO	Fluorine doped tin oxide
TiO_2	Titanium dioxide
$J–V$	Current density–voltage
J_{SC}	Short circuit current density
EQE	External quantum efficiency
IPCE	Incident photon-to-electron conversion efficiency
EIS	Electrochemical impedance spectroscopy
R_s	Series resistance
C_{rec}	Recombination chemical capacitance
R_{rec}	Recombination resistance
P	Perovskite
PbI_2	Lead iodide
FT-IR	Fourier transform infrared
^{1}H-NMR	Proton nuclear magnetic resonance
^{13}C-NMR	Carbon 13 nuclear magnetic resonance
$CDCl_3$	Deuterated chloroform
MHz	Megahertz
Anal. calcd	Calculated values of the percentage composition of a compound based on its molecular formula
ESI-MS	Electrospray ionization mass spectroscopy
DMF	Dimethylformamide
CH_2Cl_2	Dichloromethane
$MgSO_4$	Magnesium sulfate
MAI	Methylammonium iodide
XPS	X-ray photoelectron spectroscopy
TPC	Transient photocurrent technique
TPV	Transient photovoltage

Acknowledgements

References

1 S.-H. Turren-Cruz, M. Saliba, M. T. Mayer, H. Juárez-Santiesteban, X. Mathew, L. Nienhaus, W. Tress, M. P. Erodici, M.-J. Sher and M. G. Bawendi, $Energy$ $Environ.$ $Sci.$, 2018, **11**, 78–86.

2 Z. Zhu, D. Zhao, C.-C. Chueh, X. Shi, Z. Li and A. K.-Y. Jen, $Joule$, 2018, **2**, 168–183.

3   A. Farokhi, H. Shahroosvand, G. Delle Monache, M. Pilkington and M. K. Nazeeruddin, *Chem. Soc. Rev.*, 2022, **51**, 5974–6064.

4   F. Ali, C. Roldán-Carmona, M. Sohail and M. K. Nazeeruddin, *Adv. Energy Mater.*, 2020, **10**, 2002989.

5   Q. Jiang, R. Tirawat, R. A. Kerner, E. A. Gaulding, Y. Xian, X. Wang, J. M. Newkirk, Y. Yan, J. J. Berry and K. Zhu, *Nature*, 2023, **623**, 313–318.

6   C. Li, Y. Chen, Z. Zhang, C. Liu, F. Guo, W. Ahmad and P. Gao, *Energy Environ. Sci.*, 2024, **17**, 6157–6203.

7   C. Li and P. Gao, *Chin. J. Struct. Chem.*, 2024, 100324.

8   Q. Jiang and K. Zhu, *Nat. Rev. Mater.*, 2024, 1–21.

9   S. Y. Kim, S. J. Cho, S. E. Byeon, X. He and H. J. Yoon, *Adv. Energy Mater.*, 2020, **10**, 2002606.

10   E. Yalcin, M. Can, C. Rodriguez-Seco, E. Aktas, R. Pudi, W. Cambarau, S. Demic and E. Palomares, *Energy Environ. Sci.*, 2019, **12**, 230–237.

11   A. Ullah, K. H. Park, Y. Lee, S. Park, A. B. Faheem, H. D. Nguyen, Y. Siddique, K. K. Lee, Y. Jo and C. H. Han, *Adv. Funct. Mater.*, 2022, **32**, 2208793.

12   S. Casalini, C. A. Bortolotti, F. Leonardi and F. Biscarini, *Chem. Soc. Rev.*, 2017, **46**, 40–71.

13   E. Li, C. Liu, H. Lin, X. Xu, S. Liu, S. Zhang, M. Yu, X. M. Cao, Y. Wu and W. H. Zhu, *Adv. Funct. Mater.*, 2021, **31**, 2103847.

14   Y. Yao, C. Cheng, C. Zhang, H. Hu, K. Wang and S. De Wolf, *J. Adv. Mater.*, 2022, **34**, 2203794.

15   Y. Lin, Y. Firdaus, F. H. Isikgor, M. I. Nugraha, E. Yengel, G. T. Harrison, R. Hallani, A. El-Labban, H. Faber and C. Ma, *ACS Energy Lett.*, 2020, **5**, 2935–2944.

16   Z. Zhang, L. Qiao, K. Meng, R. Long, G. Chen and P. Gao, *Chem. Soc. Rev.*, 2023, **52**, 163–195.

17   S. N. Afraj, A. Velusamy, C.-Y. Chen, J.-S. Ni, Y. Ezhumalai, C.-H. Pan, K.-Y. Chen, S.-L. Yau, C.-L. Liu and C.-H. Chiang, *J. Mater. Chem. A*, 2022, **10**, 11254–11267.

18   K. Wang, J. Liu, J. Yin, E. Aydin, G. T. Harrison, W. Liu, S. Chen, O. F. Mohammed and S. De Wolf, *Adv. Funct. Mater.*, 2020, **30**, 2002861.

19   K. Sanusi, A. O. Olukoya, N. O. Sanyaolu, A. A. Ibikunle, S. T. Yussuf, S. A. Ogundare, N. O. Fatomi, O. C. Atewolara-Odule and P. B. Khoza, *J. Fluoresc.*, 2024, 1–13.

20   N. Gu, Y. Feng, L. Song, P. Zhang, P. Du, L. Ning, Z. Sun, H. Jiang and J. Xiong, *J. Mater. Chem. C*, 2023, **11**, 8942–8951.

21   Q. Liao, Y. Wang, Z. Zhang, K. Yang, Y. Shi, K. Feng, B. Li, J. Huang, P. Gao and X. Guo, *J. Energy Chem.*, 2022, **68**, 87–95.

22   T. Niu, W. Zhu, Y. Zhang, Q. Xue, X. Jiao, Z. Wang, Y.-M. Xie, P. Li, R. Chen and F. Huang, *Joule*, 2021, **5**, 249–269.

23   Y. Hua, B. Xu, P. Liu, H. Chen, H. Tian, M. Cheng, L. Kloo and L. Sun, *Chem. Sci.*, 2016, **7**, 2633–2638.

24   C. Igci, S. Paek, K. Rakstys, H. Kanda, N. Shibayama, V. Jankauskas, C. Roldán-Carmona, H. Kim, A. M. Asiri and M. K. Nazeeruddin, *Sol. RRL*, 2020, **4**, 2000173.

25   M. Jeong, I. W. Choi, E. M. Go, Y. Cho, M. Kim, B. Lee, S. Jeong, Y. Jo, H. W. Choi and J. Lee, *Science*, 2020, **369**, 1615–1620.

26   D. R. Kil, C. Lu, J.-M. Ji, C. H. Kim and H. K. Kim, *Nanomaterials*, 2020, **10**, 936.

27   L. Qian, S. Fu, S. Li, R. Miao, X. Feng, W. Zhang, Z. Xiao, W. Wang and W. Song, *J. Mater. Sci.: Mater. Electron.*, 2022, **33**, 18028–18038.

28   R. Chen, B. Long, S. Wang, Y. Liu, J. Bai, S. Huang, H. Li and X. Chen, *ACS Appl. Mater. Interfaces*, 2021, **13**, 24747–24755.

29   X. Liu, B. Ding, M. Han, Z. Yang, J. Chen, P. Shi, X. Xue, R. Ghadari, X. Zhang and R. Wang, *Angew. Chem.*, 2023, **135**, e202304350.

30   R. Singh, K. Sharma, S. B. Elavarasi and M. Guin, *Opt. Quantum Electron.*, 2024, **56**, 1002.

31   E. Rezaee, D. Khan, S. Cai, L. Dong, H. Xiao, S. R. P. Silva, X. Liu and Z.-X. Xu, *Mater. Chem. Front.*, 2023, **7**, 1704–1736.

32   W. Li, W. Zhao, K. Li and X. Han, *J. Mater. Chem. C*, 2023, **11**, 12280–12285.

33   H. Luo, Z. Zhang, L. Yuan, J. Wang, B. Li, S. Wang, M. Abdi-Jalebi, L. Shi, W. Zhang and K. Guo, *Carbon Neutrality*, 2023, **2**, 21.

34   H. Zhu, Z. Shen, L. Pan, J. Han, F. T. Eickemeyer, Y. Ren, X. Li, S. Wang, H. Liu and X. Dong, *ACS Energy Lett.*, 2020, **6**, 208–215.

35   B. Pashaei, S. Bellani, H. Shahroosvand and F. J. C. S. Bonaccorso, *Chem. Sci.*, 2020, **11**, 2429–2439.

36   M. Jeong, I. W. Choi, K. Yim, S. Jeong, M. Kim, S. J. Choi, Y. Cho, J.-H. An, H.-B. Kim and Y. Jo, *Nat. Photonics*, 2022, **16**, 119–125.

37   P. J. S. Rana, R. K. Gunasekaran, S. H. Park, V. Tamilavan, S. Karuppanan, H.-J. Kim and K. Prabakar, *J. Phys. Chem. C*, 2019, **123**, 8560–8568.

38   F. Sadeghi, B. Pashaei, B. N. Bideh, N. Sabahi, H. Shahroosvand and M. K. Nazeeruddin, *Energy Adv.*, 2023, **2**, 1693–1701.

39   Y. Tan, H. Cheng, Y. Zhao, L. Wan and Z.-S. Wang, *J. Mater. Chem. A*, 2022, **10**, 7173–7185.

40   M. Azam, T. Du, Z. Wan, H. Zhao, H. Zeng, R. Wei, C. J. Brabec, J. Luo and C. Jia, *Energy Environ. Sci.*, 2024, **17**, 6974–7016.

41   X. Ji, T. Zhou, X. Ke, W. Wang, S. Wu, M. Zhang, D. Lu, X. Zhang and Y. Liu, *J. Mater. Chem. A*, 2020, **8**, 5163–5170.

42   D. Wei, T. Wang, J. Ji, M. Li, P. Cui, Y. Li, G. Li, J. M. Mbengue and D. Song, *J. Mater. Chem. A*, 2016, **4**, 1991–1998.

43   T. Shimanouchi, H. Matsuura, Y. Ogawa and I. Harada, *J. Phys. Chem. Ref. Data*, 1978, **7**, 1323–1444.

44   S. Majidi-Nezhad, N. Sabahi, H. Shahroosvand, N. Y. Nia and A. Di Carlo, *Energy Adv.*, 2023, **2**, 1521–1530.

45   H. Choi, S. Park, S. Paek, P. Ekanayake, M. K. Nazeeruddin and J. Ko, *J. Mater. Chem. A*, 2014, **2**, 19136–19140.

46   M. Hosseini, D. E. Vanpoucke, P. Giannozzi, M. Berahman and N. Hadipour, *RSC Adv.*, 2020, **10**, 4786–4794.

47   Q. Fu, Z. Xu, X. Tang, T. Liu, X. Dong, X. Zhang, N. Zheng, Z. Xie and Y. Liu, *ACS Energy Lett.*, 2021, **6**, 1521–1532.

48   C. H. Kuan, S. N. Afraj, Y. L. Huang, A. Velusamy, C. L. Liu, T. Y. Su, X. Jiang, J. M. Lin, M. C. Chen and E. W. G. Diau, *Angew. Chem.*, 2024, e202407228.

49   L. Schein and A. McGhie, *Phys. Rev. B: Condens. Matter Mater. Phys.*, 1979, **20**, 1631.

50   W.-J. Chi, Q.-S. Li and Z.-S. Li, *Nanoscale*, 2016, **8**, 6146–6154.

51 W.-J. Chi, P.-P. Sun and Z.-S. Li, *Nanoscale*, 2016, **8**, 17752–17756.

52 H. Ashassi-Sorkhabi and P. Salehi-Abar, *Sol. Energy*, 2018, **173**, 132–138.

53 J. Wang, X. Wu, Y. Liu, T. Qin, K. Zhang, N. Li, J. Zhao, R. Ye, Z. Fan and Z. Chi, *Adv. Energy Mater.*, 2021, **11**, 2100967.

54 H. Si, S. Zhang, S. Ma, Z. Xiong, A. Kausar, Q. Liao, Z. Zhang, A. Sattar, Z. Kang and Y. Zhang, *Adv. Energy Mater.*, 2020, **10**, 1903922.

55 S. Jalili and A. Pakzadiyan, *Comput. Mater. Sci.*, 2023, **224**, 112161.

56 G. Kresse and J. Furthmüller, *Phys. Rev. B: Condens. Matter Mater. Phys.*, 1996, **54**, 11169.

57 X. Lai, F. Meng, Q. Q. Zhang, K. Wang, G. Li, Y. Wen, H. Ma, W. Li, X. Li and A. K. K. Kyaw, *Sol. RRL*, 2019, **3**, 1900011.

58 D. Bharath, M. Sasikumar, N. R. Chereddy, J. R. Vaidya and S. Pola, *Sol. Energy*, 2018, **174**, 130–138.

59 J. Xia, M. Sohail and M. K. Nazeeruddin, *Adv. Mater.*, 2023, **35**, 2211324.

60 L. Hajikhanmirzaei, H. Shahroosvand, B. Pashaei, G. Delle Monache, M. K. Nazeeruddin and M. C. Pilkington, *J. Mater. Chem. C*, 2020, **8**, 6221–6227.

61 Z. Shen, Q. Han, X. Luo, Y. Shen, Y. Wang, Y. Yuan, Y. Zhang, Y. Yang and L. J. N. P. Han, *Nat. Photonics*, 2024, 1–8.

62 A. Sun, C. Tian, R. Zhuang, C. Chen, Y. Zheng, X. Wu, C. Tang, Y. Liu, Z. Li and B. Ouyang, *Adv. Energy Mater.*, 2024, **14**, 2303941.

63 A. Abudulimu, R. Sandoval-Torrientes, I. Zimmermann, J. Santos, M. K. Nazeeruddin and N. Martín, *J. Mater. Chem. A*, 2020, **8**, 1386–1393.

64 X. Sun, F. Wang, G. Yang, X. Ding, J. Lv, Y. Sun, T. Wang, C. Gao, G. Zhang and W. Liu, *Energy Environ. Sci.*, 2025, **18**, 2536–2545.

65 A. Dualeh, T. Moehl, N. Tétreault, J. Teuscher, P. Gao, M. K. Nazeeruddin and M. Grätzel, *ACS Nano*, 2014, **8**, 362–373.

66 H.-S. Kim, I. Mora-Sero, V. Gonzalez-Pedro, F. Fabregat-Santiago, E. J. Juarez-Perez, N.-G. Park and J. Bisquert, *Nat. Commun.*, 2013, **4**, 2242.

67 Q. Liao, Y. Wang, Z. Zhang, K. Yang, Y. Shi, K. Feng, B. Li, J. Huang, P. Gao and X. Guo, *J. Energy Chem.*, 2022, **68**, 87–95.

68 K. Yang, Q. Liao, J. Huang, Z. Zhang, M. Su, Z. Chen, Z. Wu, D. Wang, Z. Lai and H. Y. Woo, *Angew. Chem., Int. Ed.*, 2022, **61**, e202113749.

69 L. Duan, Y. Chen, J. Yuan, X. Zong, Z. Sun, Q. Wu and S. Xue, *Dyes Pigm.*, 2020, **178**, 108334.

70 K. Rakstys, S. Paek, P. Gao, P. Gratia, T. Marszalek, G. Grancini, K. T. Cho, K. Genevicius, V. Jankauskas and W. Pisula, *J. Mater. Chem. A*, 2017, **5**, 7811–7815.

71 S. Zhang, R. Wu, C. Mu, Y. Wang, L. Han, Y. Wu and W.-H. Zhu, *ACS Mater. Lett.*, 2022, **4**, 1976–1983.

72 Q. Liao, Y. Wang, M. Hao, B. Li, K. Yang, X. Ji, Z. Wang, K. Wang, W. Chi and X. Guo, *ACS Appl. Mater. Interfaces*, 2022, **14**, 43547–43557.

73 S. N. Afraj, C. H. Kuan, J. S. Lin, J. S. Ni, A. Velusamy, M. C. Chen and E. W. G. Diau, *Adv. Funct. Mater.*, 2023, **33**, 2213939.

74 I. Mesquita, L. Andrade and A. J. C. Mendes, *ChemSusChem*, 2019, **12**, 2186–2194.

75 Y. Fang, X. Wang, Q. Wang, J. Huang and T. Wu, *Phys. Status Solidi*, 2014, **211**, 2809–2816.

76 H. Zheng, G. Liu, C. Zhang, L. Zhu, A. Alsaedi, T. Hayat, X. Pan and S. Dai, *Sol. Energy*, 2018, **159**, 914–919.

77 S. Akin, M. Bauer, R. Uchida, N. Arora, G. Jacopin, Y. Liu, D. Hertel, K. Meerholz, E. Mena-Osteritz and P. Bäuerle, *ACS Appl. Energy Mater.*, 2020, **3**, 7456–7463.

78 M. Petrus, T. Bein, T. Dingemans and P. Docampo, *J. Mater. Chem. A*, 2015, **3**, 12159–12162.

79 B. Xu, D. Bi, Y. Hua, P. Liu, M. Cheng, M. Grätzel, L. Kloo, A. Hagfeldt and L. Sun, *Energy Environ. Sci.*, 2016, **9**, 873–877.

80 M. Saliba, S. Orlandi, T. Matsui, S. Aghazada, M. Cavazzini, J.-P. Correa-Baena, P. Gao, R. Scopelliti, E. Mosconi and K.-H. Dahmen, *Nat. Energy*, 2016, **1**, 1–7.

81 T. P. Osedach, T. L. Andrew and V. Bulović, *Energy Environ. Sci.*, 2013, **6**, 711–718.

82 B. Pashaei, H. Shahroosvand, M. Ameri, E. Mohajerani and M. K. Nazeeruddin, *J. Mater. Chem. A*, 2019, **7**, 21867–21873.

83 Z. Zaman, H. Shahroosvand, S. Bellani, F. Bonaccorso and M. K. Nazeeruddin, *Angew. Chem., Int. Ed.*, 2025, **64**, e202425191.